Maneuvering Target Tracking Using Continuous Wave Bistatic Sonar with Propagation Delay

Rong Yang, Yaakov Bar-Shalom, Claude Jauffret, Annie-Claude Perez, Gee Wah Ng

Maneuvering Target Tracking Using Continuous Wave Bistatic Sonar with Propagation Delay

Rong Yang

Yaakov Bar-Shalom

Claude Jauffret

Annie-Claude Pérez

Gee Wah Ng

Abstract

Acoustic propagation delay has not been investigated for a continuous wave multistatic sonar tracking system except for the recent study conducted by Jauffret et al. [6], which estimates the trajectory of a constant velocity target. The results showed that the estimate bias caused by the propagation delay is not negligible, especially for a bistatic system. This paper develops an interacting multiple model unscented Gauss-Helmert filter with numerical Jacobian (IMM-UGHF-NJ) to track a maneuvering target with propagation delay using a bistatic sonar system. The IMM-UGHF-NJ can overcome the two tracking challenges introduced by the delay, namely, implicit state transition model and lack of analytical expression of the Doppler shifted frequency in the measurement model. Simulation tests have been conducted, and the results show that the IMM-UGHF-NJ can reduce the estimation error significantly, especially for long range or fast moving targets.

Rong Yang and Gee Wah Ng are with DSO National Laboratories, 20 Science Park Drive, Singapore 118230. E-mails: yrong@dso.org.sg; ngeewah@dso.org.sg.

Yaakov Bar-Shalom is with Department of ECE, University of Connecticut, Storrs, CT 06269, USA. Supported by ARO Grant W911NF-10-1-0369. E-mail: ybs@engr.uconn.edu.

Claude Jauffret and Annie-Claude Pérez are with University of Toulon, IM2NP, UMR7334, CS 60584, 83041 TOULON Cedex, France. E-mails: jauffret@univ-tln.fr; annie-claude.perez@univ-tln.fr

Maneuvering Target Tracking Using Continuous Wave Bistatic Sonar with Propagation Delay

I. Introduction

Continuous active sonar (CAS), also known as high duty cycle (HDC) sonar, with multistatic setup has attracted the research interest recently. In such a system, the signal is transmitted almost in a full duty cycle. Compared to the commonly used pulse active sonar (PAS) system, which transmits only a short pulse in a cycle, the CAS system has continuous detection capability, and is less disturbing to underwater fauna through using a low intensity signal.

There are two main types of CAS systems according to the signal waveforms transmitted, namely, frequency modulated (FM) waveforms and continuous constant frequency waveforms (CW). The FM-CAS can provide good target bistatic range information, whereas the CW-CAS has good Doppler shifted frequency measurement (linked to target range rate). The FM-CAS needs to separate indirect path signal from strong direct path signal via methods, such as m-sequence modulation [3] and Dopplergram [10]. The FM-CAS has a frequency bandwidth limitation issue in multistatic system, as broadband waveforms are transmitted repeatedly [5]. The CW-CAS transmits a single fixed frequency waveform, so that it has no frequency bandwidth limitation problem as the FM-CAS. However, due to lack of range information, the observability of a target trajectory in CW-CAS is not as good as FM-CAS, especially for bistatic (a single transmitter-receiver pair) system.

We focus on target tracking using CW-CAS in this paper. A few approaches on this problem have been proposed in literature before. A Gaussian mixture probability hypothesis density (GMPHD) filter was developed in [5]. It tracks multiple constant velocity (CV) targets using bearings and Doppler frequencies detected by multistatic CW-CAS. Results show that CV targets can be tracked using more than two transmitter-receiver pairs when target range is not available. This research does not take signal propagation delay into consideration. The effect of propagation delay of CW-CAS has been studied in [6] recently. An exact Doppler frequency model with propagation delay was proposed. and a maximum likelihood (ML) estimator based on this model was developed to perform batch estimation for a CV target. The simulation results showed that the estimation bias induced by the propagation delay is not negligible, especially for a bistatic system.

In this paper, the propagation delay problem raised in [6] is studied further. We extend the target CV trajectory estimation using a batch parameter estimation technique to the dynamic recursive

estimation, which can handle not only CV motion but also maneuvering motion. This extension faces two challenges. Firstly, the "target time" t_k and target position (x_k,y_k) in the state [defined later in (1) and (2)] are highly correlated after propagation delay is introduced. This leads to a state transition equation in an implicit form instead of the commonly used explicit form in [11][12]. Secondly, the Doppler shifted frequency (one of the measurements) does not have an analytical expression in terms of the target state. This is because the Doppler frequency is a function of the bistatic range rate which cannot be described analytically after propagation delay is introduced. Details will be given later in Section II-B. The two challenges mentioned above were overcome in [6] through solving a 2nd order polynomial equation for CV target. However, the approach in [6] cannot be applied to a maneuvering target with coordinated turn (CT) motion, and the new approach in this paper will be shown to handle this.

A dynamic estimation problem uses two basic models, namely, the state transition model and the measurement model. The state transition model describes the evolution of the target state with time, and it is (in most cases) an explicit expression of the state at the current time in terms of the state at the previous time. The measurement model relates the measurement to the state. The two challenges of the dynamic estimation problem considered in this paper are: (i) the implicit state transition model; (ii) the lack of an analytical measurement model. These make this problem impossible to solve using existing filters.

We will develop an interacting multiple model unscented Gauss-Helmert filter with numerical Jacobian (IMM-UGHF-NJ) to cope with the challenges mentioned above. The IMM [2] is a well known hybrid algorithm to handle motion model uncertainty in maneuvering target tracking. The UGHF [11][12][14][15] is a recently developed algorithm for bearings-only tracking (BOT) with implicit state transition model introduced by the acoustic propagation delay. It can be applied to our problem. For the measurement model without analytical form, the NJ (numerical Jacobian) algorithm, which computes the Jacobian numerically, can be utilized [8][13][9]. The Doppler shifted frequency is a function of the bistatic range rate, $\dot{r}$, which has no analytical form due to the unknown time delay. We can compute $\dot{r}$ (derivative of range r) using the NJ.

The structure of the rest of paper is as follows. Section II formulates the problem. Section III presents the IMM-UGHF-NJ. Simulation results and conclusions are in Sections IV and V, respectively.

II. Problem Formulation

The problem is illustrated in Fig. 1. At dynamic estimation cycle k, the transmitter emits a CW signal with constant frequency f^{T} at time t_k^{T}, and the receiver receives the Doppler shifted frequency f^{R} at time t_k^{R} via the target reflection at time t_k. We assume the transmitter and receiver are stationary

and located at $(x^{\mathrm{T}},y^{\mathrm{T}})$ and $(x^{\mathrm{R}},y^{\mathrm{R}})$, respectively. The target is moving and its location is $[x(t_k),y(t_k)]$ at reflection time t_k. The ranges between the target at t_k to the transmitter and the receiver are r_k^{T} and r_k^{R}, respectively.

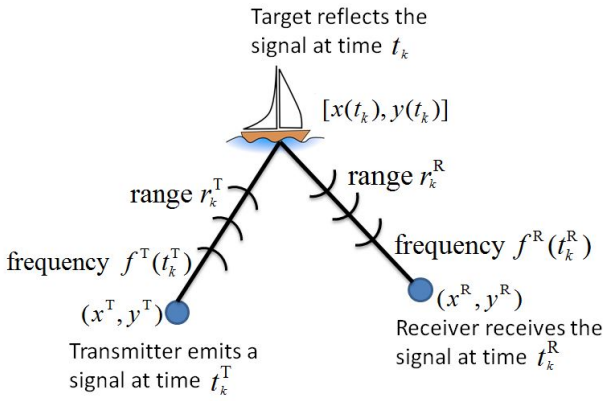

Fig. 1. Signal transmission of CW bistatic sonar.

The target states to be estimated for the CV and CT models at time t_k are

$$\mathbf{x}^{\mathrm{CV}}(t_k) = [x(t_k) \;\; y(t_k) \;\; \dot{x}(t_k) \;\; \dot{y}(t_k) \;\; t_k]' \tag{1}$$

$$\mathbf{x}^{\mathrm{CT}}(t_k) = [x(t_k) \;\; y(t_k) \;\; \dot{x}(t_k) \;\; \dot{y}(t_k) \;\; \omega(t_k) \;\; t_k]' \tag{2}$$

where x, y, $\dot{x}$ and $\dot{y}$ are the target positions and velocities in the x and y coordinates, respectively, ω is the target turn rate, and t_k is the target time (or reflection time) corresponding to the emission time t_k^{T} and the reception time t_k^{R} of the transmitter and receiver, respectively. The measurement vector at time t_k^{R} is

$$\mathbf{z}(t_k^{\mathrm{R}}) = [b(t_k^{\mathrm{R}}) \;\; f^{\mathrm{R}}(t_k^{\mathrm{R}})]' \tag{3}$$

where b is the target bearing from the receiver at time t_k^{R} to the target at time t_k, measured clockwise from True North, and f^{R} is the Doppler shifted frequency at the receiver.

A. State transition models

The state transition model describes the evolution of the target state with time. For a generic discrete problem, it is an explicit form given by

$$\mathbf{x}(t_k) = \mathbf{f}[\mathbf{x}(t_{k-1})] + \Gamma\mathbf{v}(t_{k-1}) \tag{4}$$

where k is the discrete estimation cycle index, $\mathbf{v}(t_{k-1})$ is the process noise, and Γ is the process noise gain. However, there is no explicit state transition model for our problem. It can be seen from

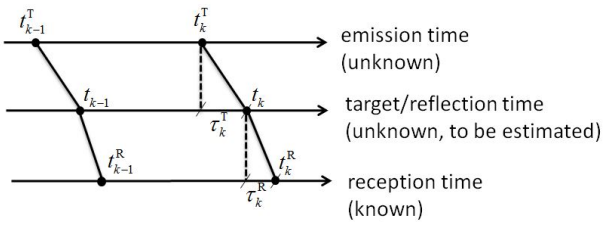

Fig. 2. Time sequences of continuous wave bistatic sonar.

Fig. 2 that the target time, t_k, is unknown due to the unknown propagation delay τ^{R}. There is an implicit constraint between the known t^{R}_k and unknown t_k given by

$$t_k = t^{\mathrm{R}}_k - \tau^{\mathrm{R}}_k \tag{5}$$

where

$$\tau^{\mathrm{R}}_k = \frac{\sqrt{[x(t_k) - x^{\mathrm{R}}]^2 + [y(t_k) - y^{\mathrm{R}}]^2}}{c^{\mathrm{p}}} \tag{6}$$

and c^{p} is the signal propagation speed in the medium. It can be seen that t_k is on the both sides of the constraint equation (5), since $x(t_k)$ and $y(t_k)$ are functions of t_k. It is difficult to obtain an explicit express of t_k. This leads to use a Gauss-Helmert (GH) state transition model, which describes an implicit constraint systemically [11][12]. The GH model is given by

$$\mathbf{g}[\mathbf{x}(t_k), \mathbf{x}(t_{k-1})] + \Gamma \mathbf{v}(t_{k-1}) = \mathbf{0} \tag{7}$$

The GH models for the CV motion[1] and CT motion are given next.

1) Constant velocity Gauss-Helmert model

The GH model for CV motion is given by

$$\mathbf{g}^{\mathrm{CV}}\left[\mathbf{x}^{\mathrm{CV}}(t_k), \mathbf{x}^{\mathrm{CV}}(t_{k-1})\right] + \Gamma^{\mathrm{CV}} \mathbf{v}^{\mathrm{CV}}(t_{k-1}) = \mathbf{0}_5 \tag{8}$$

where $\mathbf{g}^{\mathrm{CV}}[\cdot]$ is the implicit GH state transition function, which combines the CV motion constraints and the delay constraint between $\mathbf{x}(t_k)$ and $\mathbf{x}(t_{k-1})$. It is given by

$$\mathbf{g}^{\mathrm{CV}}(\cdot) = \left[g^{\mathrm{CV}}_1(\cdot)\ g^{\mathrm{CV}}_2(\cdot)\ g^{\mathrm{CV}}_3(\cdot)\ g^{\mathrm{CV}}_4(\cdot)\ g^{\mathrm{CV}}_5(\cdot)\right]' \tag{9}$$

[1]Although an explicit state transition model for the CV motion can be obtained through solving a 2nd order polynomial equation [6], the GH model is a systematical way which is suitable for both CV and CT motions.

where

$$g_1^{\mathrm{CV}}(\cdot) = x(t_k) - [x(t_{k-1}) + \dot{x}(t_{k-1})\Delta_k] \tag{10}$$

$$g_2^{\mathrm{CV}}(\cdot) = y(t_k) - [y(t_{k-1}) + \dot{y}(t_{k-1})\Delta_k] \tag{11}$$

$$g_3^{\mathrm{CV}}(\cdot) = \dot{x}(t_k) - \dot{x}(t_{k-1}) \tag{12}$$

$$g_4^{\mathrm{CV}}(\cdot) = \dot{y}(t_k) - \dot{y}(t_{k-1}) \tag{13}$$

$$g_5^{\mathrm{CV}}(\cdot) = t_k - (t_k^{\mathrm{R}} - \tau_k^{\mathrm{R}}) \tag{14}$$

with τ_k^{R} given in (6) and

$$\Delta_k = t_k - t_{k-1} \tag{15}$$

Based on the discrete white noise acceleration (WNA) model [2], the gain matrix Γ^{CV} and the zero-mean white Gaussian process noise $\mathbf{v}^{\mathrm{CV}}$ in (8) compensate for small accelerations and the uncertainty of the sound speed. The noise gain matrix Γ^{CV} is given by

$$\Gamma^{\mathrm{CV}} = \begin{bmatrix} \frac{1}{2}(\Delta_k)^2 & 0 & 0 \\ 0 & \frac{1}{2}(\Delta_k)^2 & 0 \\ \Delta_k & 0 & 0 \\ 0 & \Delta_k & 0 \\ 0 & 0 & 1 \end{bmatrix} \tag{16}$$

The covariance of $\mathbf{v}^{\mathrm{CV}}$ is

$$\mathbf{q}^{\mathrm{CV}} = \mathrm{diag}(\sigma_{\dot{\mathrm{x}}}^2 \;\; \sigma_{\dot{\mathrm{y}}}^2 \;\; \sigma_{\mathrm{t}}^2) \tag{17}$$

where $\sigma_{\dot{x}}^2$ and $\sigma_{\dot{y}}^2$ are the variances on small target accelerations in the x and y coordinates respectively, and σ_t^2 is the process noise variance on the target time. The covariance of the error in the model (8) is given by

$$\mathbf{Q}^{\mathrm{CV}}(\Delta_k) = \Gamma^{\mathrm{CV}}\mathbf{q}^{\mathrm{CV}}(\Gamma^{\mathrm{CV}})' \tag{18}$$

2) Coordinated Turn Gauss-Helmert model

The GH state transition model for the CT motion is given by

$$\mathbf{g}^{\mathrm{CT}}[\mathbf{x}^{\mathrm{CT}}(t_k), \mathbf{x}^{\mathrm{CT}}(t_{k-1})] + \Gamma^{\mathrm{CT}}\mathbf{v}^{\mathrm{CT}}(t_{k-1}) = \mathbf{0}_6 \tag{19}$$

where

$$\mathbf{g}^{\mathrm{CT}}(\cdot) = \left[g_1^{\mathrm{CT}}(\cdot)\; g_2^{\mathrm{CT}}(\cdot)\; g_3^{\mathrm{CT}}(\cdot)\; g_4^{\mathrm{CT}}(\cdot)\; g_5^{\mathrm{CT}}(\cdot)\; g_6^{\mathrm{CT}}(\cdot)\right]' \tag{20}$$

with

$$\begin{aligned} g_1^{\mathrm{CT}}(\cdot) &= x(t_k) - \Big[x(t_{k-1}) + \frac{\sin[\omega(t_{k-1})\Delta_k]}{\omega(t_{k-1})}\dot{x}(t_{k-1}) \\ &\quad - \frac{1-\cos[\omega(t_{k-1})\Delta_k]}{\omega(t_{k-1})}\dot{y}(t_{k-1})\Big] \qquad (21) \\ g_2^{\mathrm{CT}}(\cdot) &= y(t_k) - \Big[y(t_{k-1}) + \frac{\sin[\omega(t_{k-1})\Delta_k]}{\omega(t_{k-1})}\dot{y}(t_{k-1}) \\ &\quad + \frac{1-\cos[\omega(t_{k-1})\Delta_k]}{\omega(t_{k-1})}\dot{x}(t_{k-1})\Big] \qquad (22) \\ g_3^{\mathrm{CT}}(\cdot) &= \dot{x}(t_k) - \{\cos[\omega(t_{k-1})\Delta_k]\dot{x}(t_{k-1}) \\ &\quad - \sin[\omega(t_{k-1})\Delta_k]\dot{y}(t_{k-1})\} \qquad (23) \\ g_4^{\mathrm{CT}}(\cdot) &= \dot{y}(t_k) - \{\sin[\omega(t_{k-1})\Delta_k]\dot{x}(t_{k-1}) \\ &\quad + \cos[\omega(t_{k-1})\Delta_k]\dot{y}(t_{k-1})\} \qquad (24) \\ g_5^{\mathrm{CT}}(\cdot) &= \omega(t_k) - \omega(t_{k-1}) \qquad (25) \\ g_6^{\mathrm{CT}}(\cdot) &= t_k - (t_k^{\mathrm{R}} - \tau_k^{\mathrm{R}}) \qquad (26) \end{aligned}$$

The noise gain matrix Γ^{CT} is given by

$$\Gamma^{\mathrm{CT}} = \begin{bmatrix} \frac{1}{2}(\Delta_k)^2 & 0 & 0 & 0 \\ 0 & \frac{1}{2}(\Delta_k)^2 & 0 & 0 \\ \Delta_k & 0 & 0 & 0 \\ 0 & \Delta_k & 0 & 0 \\ 0 & 0 & \Delta_k & 0 \\ 0 & 0 & 0 & 1 \end{bmatrix} \qquad (27)$$

$$\mathbf{q}^{\mathrm{CT}} = \mathrm{diag}(\sigma_{\dot{x}}^2 \;\; \sigma_{\ddot{y}}^2 \;\; \sigma_{\omega}^2 \;\; \sigma_t^2) \qquad (28)$$

where σ_ω^2 is the variance of the Gaussian process noises of ω. The covariance of the error in (19) for the (nearly) CT motion, $\mathbf{Q}^{\mathrm{CT}}(\Delta_k)$, is computed by

$$\mathbf{Q}^{\mathrm{CT}}(\Delta_k) = \Gamma^{\mathrm{CT}}\mathbf{q}^{\mathrm{CT}}(\Gamma^{\mathrm{CT}})' \qquad (29)$$

B. Measurement model

The measurement model relates the state at time t_k to the measurement at time t_k^{R}, which is given by

$$\mathbf{z}(t_k^{\mathrm{R}}) = \mathbf{h}[\mathbf{x}(t_k)] + \mathbf{w}(t_k^{\mathrm{R}}) \qquad (30)$$

where $\mathbf{w}(t_k^{\mathrm{R}})$ is the measurement noise, and

$$\mathbf{h}(\cdot) = [h_1(\cdot)\ h_2(\cdot)]' \tag{31}$$

with

$$h_1(\cdot) = b(t_k^{\mathrm{R}}) = \tan^{-1}\left[\frac{x(t_k) - x^{\mathrm{R}}}{y(t_k) - y^{\mathrm{R}}}\right] \tag{32}$$

$$h_2(\cdot) = f^{\mathrm{R}}(t_k^{\mathrm{R}}) = f^{\mathrm{T}}(t_k^{\mathrm{T}})\left[1 - \frac{\dot{r}(t_k^{\mathrm{R}})}{c^{\mathrm{P}}}\right] \tag{33}$$

The challenge is how to obtain $\dot{r}(t_k^{\mathrm{R}})$ in (33). We know

$$\begin{aligned} r(t_k^{\mathrm{R}}) &= r_k^{\mathrm{T}} + r_k^{\mathrm{R}} \\ &= \sqrt{[x(t_k) - x^{\mathrm{T}}]^2 + [y(t_k) - y^{\mathrm{T}}]^2} \\ &\quad + \sqrt{[x(t_k) - x^{\mathrm{R}}]^2 + [y(t_k) - y^{\mathrm{R}}]^2} \end{aligned} \tag{34}$$

and

$$\begin{aligned} \dot{r}(t_k^{\mathrm{R}}) &= \frac{d[r(t_k^{\mathrm{R}})]}{d(t_k^{\mathrm{R}})} \\ &= \frac{\dot{x}(t_k)[x(t_k) - x^{\mathrm{T}}] + \dot{y}(t_k)[y(t_k) - y^{\mathrm{T}}]}{r_k^{\mathrm{T}}}\frac{dt_k}{d(t_k^{\mathrm{R}})} \\ &\quad + \frac{\dot{x}(t_k)[x(t_k) - x^{\mathrm{R}}] + \dot{y}(t_k)[y(t_k) - y^{\mathrm{R}}]}{r_k^{\mathrm{R}}}\frac{dt_k}{d(t_k^{\mathrm{R}})} \end{aligned} \tag{35}$$

When the signal propagation delay is negligible (for example, for a radar signal), one has $t_k = t_k^{\mathrm{R}}$ and

$$\frac{dt_k}{d(t_k^{\mathrm{R}})} = 1 \tag{36}$$

The analytical form of $\dot{r}(t_k^{\mathrm{R}})$ is then

$$\begin{aligned} \dot{r}(t_k^{\mathrm{R}}) &= \frac{\dot{x}(t_k)[x(t_k) - x^{\mathrm{T}}] + \dot{y}(t_k)[y(t_k) - y^{\mathrm{T}}]}{r_k^{\mathrm{T}}} \\ &\quad + \frac{\dot{x}(t_k)[x(t_k) - x^{\mathrm{R}}] + \dot{y}(t_k)[y(t_k) - y^{\mathrm{R}}]}{r_k^{\mathrm{R}}} \end{aligned} \tag{37}$$

However, the acoustic signal in our problem has significant propagation delay and $t_k \neq t_k^{\mathrm{R}}$. The analytical function

$$t_k = f(t_k^{\mathrm{R}}) \tag{38}$$

is impossible to obtain for a target in CT motion. This causes a major challenge for mapping the state to the measurement. An appropriate filter to cope with this challenge will be developed next.

III. Interacting Multiple Model Unscented Gauss-Helmert Filter with Numerical Jacobian

The IMM estimator [2] is the most commonly used hybrid approach to handle model uncertainty in target tracking. This section describes an IMM-UGHF-NJ filter with the implicit CV and CT models described in Section II and lack of analytical expression for the measurement function.

Similarly to the original IMM estimator, the IMM-UGHF-NJ performs the state estimation in four steps: mixing, mode-matched filtering, mode probabilities updating and final state combination:

1) In the mixing step, the m hypotheses (where m is the number of models in the filter) at time k-1 expand to m^2 hypotheses using the mixing probabilities based on the mode Markov chain, which is governed by the $m \times m$ mode probability transition matrix Π consisting of the mode transition probabilities, p_{ij}. The m^2 hypotheses are then merged into m hypotheses based on the mixture equations [2].
2) In the mode-matched filtering step, the mixed state estimates are updated by UGHF-NJs (given later) in parallel.
3) The mixing probabilities are obtained, and the updated mode probabilities are computed based on the innovations in the mode-matched UGHF-NJs. The updated mode probabilities together with the mode-conditioned estimated states and covariances are brought to the next step.
4) The final state estimate and its covariance for the current time cycle are computed based on the mixture equations using the latest mode probabilities in the combination step.

Since the states in the CV and CT models described in Section II have different dimensions, the unbiased mixing approach [16] is applied in the IMM filter to increase the CV state from 5 to 6. Before the mixing step, the CV state estimate and its error covariance are augmented with the turn rate information from the CT model.

The IMM-UGHF-NJ differs from the standard IMM in the mode-matched filters, which are UGHF-NJ. The UGHF-NJ handles the implicit GH state transition model and evaluates $f^{\mathrm{R}}(t_k^{\mathrm{R}})$ in the measurement vector (3) numerically. The UGHF-NJ prediction, state-to-measurement mapping and update steps are given in Algorithms 1–3, respectively. In these algorithms, the model superscripts "CV" and "CT" for the states and GH functions are omitted for simplicity.

Algorithm 1 predicts the state $\hat{\mathbf{x}}(\hat{t}_{k-1})$ from time $\hat{t}_{k-1}$ to an unknown target time, t_k, corresponding to the signal reception time t_k^{R}. The relationship between t_k and t_k^{R} is given by the implicit constraint (5). An unscented Gauss-Helmert approach is used for the state prediction with the implicit constraint. Firstly, $2n_{\mathbf{x}} + 1$ sigma points of $\hat{\mathbf{x}}(\hat{t}_{k-1})$ are generated using $\mathrm{SigPt}(\cdot)$ (given in the

Algorithm 1 UGHF-NJ prediction

Generate $(2n_{\mathbf{x}}+1)$ sigma points for $\hat{\mathbf{x}}(t_{k-1})$:

$$[\{\hat{\mathbf{x}}^i(\hat{t}^i_{k-1})\},\{w^i\}] = \mathrm{SigPt}[\hat{\mathbf{x}}(\hat{t}_{k-1}),\mathbf{P}(\hat{t}_{k-1}),\kappa]$$

Predict sigma points using Gauss-Newton algo.:

for all $\hat{\mathbf{x}}^i(\hat{t}^i_{k-1})$, $i\in\{1,\ldots,2n_{\mathbf{x}}+1\}$ **do**

$$\mathbf{x}_0 = \hat{\mathbf{x}}^i(\hat{t}^i_{k-1})$$

$$\breve{\mathbf{x}}^i(\hat{t}^i_k|\hat{t}^i_{k-1}) = \mathrm{GaussN}[\mathbf{g}(\mathbf{x}_1,\mathbf{x}_0)]$$

end for

Regen sigma points with process noise:

$$\hat{\mathbf{x}}(\hat{t}_k|\hat{t}_{k-1}) = \sum_{i=1}^{2n_{\mathbf{x}}+1} w^i\breve{\mathbf{x}}^i(\hat{t}^i_k|\hat{t}^i_{k-1})$$

$$\mathbf{P}(\hat{t}_k|\hat{t}_{k-1}) = \sum_{i=1}^{2n_{\mathbf{x}}+1} w^i\tilde{\mathbf{x}}^i(\hat{t}^i_k|\hat{t}^i_{k-1})(\tilde{\mathbf{x}}^i(\hat{t}^i_k|\hat{t}^i_{k-1}))' + \mathbf{Q}(\Delta_k)$$

$$[\{\hat{\mathbf{x}}^i(\hat{t}^i_k|\hat{t}^i_{k-1})\},\{w^i\}] = \mathrm{SigPt}[\hat{\mathbf{x}}(\hat{t}_k|\hat{t}_{k-1}),\mathbf{P}(\hat{t}_k|\hat{t}_{k-1}),\kappa]$$

where

$$\tilde{\mathbf{x}}^i(\hat{t}^i_k|\hat{t}^i_{k-1}) = \breve{\mathbf{x}}^i(\hat{t}^i_k|\hat{t}^i_{k-1}) - \hat{\mathbf{x}}(\hat{t}_k|\hat{t}_{k-1})$$

κ is a spread scalar of the sigma points.

Appendix), where $n_{\mathbf{x}}$ is the dimension of the state vector. Secondly, each sigma point is predicted to $\hat{t}^i_k$ using the Gauss-Newton algorithm $\mathrm{GaussN}(\cdot)$ (also given in the Appendix) based on the Gauss-Helmert function $\mathbf{g}(\mathbf{x}_1,\mathbf{x}_0)$, where i is the index of the sigma points. The $2n_{\mathbf{x}}+1$ $\mathrm{GaussN}(\cdot)$ find $\mathbf{x}_1 = \breve{\mathbf{x}}^i(\hat{t}^i_k|\hat{t}^i_{k-1})$ from $\mathbf{x}_0 = \hat{\mathbf{x}}^i(\hat{t}^i_{k-1})$ iteratively. Thirdly, the predicted sigma points are re-generated with considering also the process noise (with the approprate larger prediction covariance).

Algorithm 2 maps the predicted state to the measurement space. The challenge here is that we cannot obtain the Doppler shifted frequency $f^{\mathrm{R}}(t^{\mathrm{R}}_k)$ in the measurement from the predicted state directly. The range rate $\dot{r}(t^{\mathrm{R}}_k)$ in (33) cannot be derived from the bistatic range $r(t^{\mathrm{R}}_k)$, which has no analytical form in terms of t^{R}_k. We use an numerical approach, called numerical Jacobian (NJ), to obtain $\dot{r}(t^{\mathrm{R}}_k)$ from $r(t^{\mathrm{R}}_k)$. It is known that the slope of the tangent line is the derivative of a nonlinear function at a point of interest. The principle of the $\mathrm{NJ}(\cdot)$ (given in the Appendix) is to find the best linear fit to a nonlinear function based on a few weighted points around the point of interest. If we can provide these weighted points around $[t^{\mathrm{R}}_k, r(t^{\mathrm{R}}_k)]$, its derivative $\dot{r}(t^{\mathrm{R}}_k)$ can then be computed using $\mathrm{NJ}(\cdot)$. Firstly, we generate the reception time set around t^{R}_k using $\mathrm{SigPt}(\cdot)$, i.e.,

$$\{t^{\mathrm{R},j}_k\} = \{t^{\mathrm{R}}_k, t^{\mathrm{R}}_k - \sigma_{t^{\mathrm{R}}_k}, t^{\mathrm{R}}_k + \sigma_{t^{\mathrm{R}}_k}\} \quad j=1,2,3 \tag{39}$$

Algorithm 2 UGHF-NJ mapping the predicted state to measurement

$[\{t_k^{\mathrm{R},j}\},\{w^j\}] = \mathrm{SigPt}[t_k^{\mathrm{R}}, \sigma_{t_k^{\mathrm{R}}}, \kappa]$
for all $\hat{\mathbf{x}}^i(\hat{t}_k^i|\hat{t}_{k-1}^i)$, $i \in \{1,\ldots,2n_{\mathbf{x}}+1\}$ **do**
  $\mathbf{x}_0 = \hat{\mathbf{x}}^i(\hat{t}_k^i|\hat{t}_{k-1}^i)$
  for $j = 1:3$ **do**
    $\hat{\mathbf{x}}^{i,j}(\hat{t}_k^j|\hat{t}_{k-1}^i) = \mathrm{GaussN}\left[\mathbf{g}(\mathbf{x}_1,\mathbf{x}_0)|_{t_k^{\mathrm{R}}=t_k^{\mathrm{R},j}}\right]$
    $\hat{r}^{i,j}(t_k^{\mathrm{R}}) \leftarrow \hat{\mathbf{x}}^{i,j}(\hat{t}_k^j|\hat{t}_{k-1}^i)$
  end for
  $\hat{\dot{r}}^i(t_k^{\mathrm{R}}) = \mathrm{NJ}[\{t_k^{\mathrm{R},j}\},\{\hat{r}^{i,j}(t_k^{\mathrm{R}})\},\{w^j\}]$
  $\hat{f}^{\mathrm{R},i}(t_k^{\mathrm{R}}) \leftarrow$ using (33)
  $\hat{b}^i(t_k^{\mathrm{R}}) \leftarrow$ using (32)
  $\mathbf{z}^i(t_k^{\mathrm{R}}) = [\hat{b}^i(t_k^{\mathrm{R}})\ \hat{f}^{\mathrm{R},i}(t_k^{\mathrm{R}})]'$
end for
$\hat{\mathbf{z}}(t_k^{\mathrm{R}}) = \sum_{i=1}^{2n_{\mathbf{x}}+1} w^i \hat{\mathbf{z}}^i(t_k^{\mathrm{R}})$

where $\sigma_{t_k^{\mathrm{R}}}$ is a very small shift from t_k^{R}. Its weight set is $\{w^j\}$. Secondly, we use $\mathrm{GaussN}(\cdot)$ to obtain the predicted state set $\{\hat{\mathbf{x}}^{i,j}(\hat{t}_k|\hat{t}_{k-1})\}$ corresponding to the reception time set $\{t_k^{\mathrm{R},j}\}$ for the ith sigma point of the predicted state (obtained from Algorithm 1). The bistatic range can then be computed using (34). The set of bistatic ranges corresponding to $\{t_k^{\mathrm{R},j}\}$ for the ith sigma point of the predicted state is

$$\{\hat{r}^{i,j}(t_k^{\mathrm{R}})\} = \{\hat{r}^i(t_k^{\mathrm{R}}), \hat{r}^i(t_k^{\mathrm{R}} - \sigma_{t_k^{\mathrm{R}}}), \hat{r}^i(t_k^{\mathrm{R}} + \sigma_{t_k^{\mathrm{R}}})\} \quad j = 1,2,3 \tag{40}$$

Thirdly, we use these two sets, $\{t_k^{\mathrm{R},j}\}$ and $\{\hat{r}^{i,j}(t_k^{\mathrm{R}})\}$, which form three points around $[t_k^{\mathrm{R}}, \hat{r}^i(t_k^{\mathrm{R}})]$ to evaluate the range rate $\hat{\dot{r}}^i(t_k^{\mathrm{R}})$ using $\mathrm{NJ}(\cdot)$. Once $\hat{\dot{r}}^i(t_k^{\mathrm{R}})$ is obtained, $f^{\mathrm{R},i}(t_k^{\mathrm{R}})$ can be computed using (33), and the predicted measurement $\mathbf{z}^i(t_k^{\mathrm{R}})$ follows.

Algorithm 3 updates the predicted state based on the measurment $\mathbf{z}(t_k^{\mathrm{R}})$. This step is the same as in the conventional UKF.

IV. Simulation Results

The IMM-UGHF-NJ is tested with simulated data in this section. The simulated scenarios are shown in Fig. 3. Twelve targets move in CV-CT-CV motion with different speeds and ranges. They are categorised into four groups based on the ranges (or distances) to the transmitter and receiver, which are between 0–5km, 5–10km, 10–15km and 15–20km. Each category has three targets with speeds 10m/s, 20m/s and 30m/s, respectively. All targets have two CV legs linked by a CT arc. The durations of the first CV, CT and the second CV are 90s, 45s and 90s, respectively. The CT arc is a 90$^{\mathrm{o}}$ right turn with turn rate 2$^{\mathrm{o}}$/s. The transmitter and receiver are located at (-3500m,0m) and

Algorithm 3 UGHF-NJ update

$$\hat{\mathbf{x}}(\hat{t}_k) = \hat{\mathbf{x}}(\hat{t}_k|\hat{t}_{k-1}) + \mathbf{K}_k\nu(t_k^{\mathrm{R}})$$
$$\mathbf{P}(\hat{t}_k) = \mathbf{P}(\hat{t}_k|\hat{t}_{k-1}) - \mathbf{K}_k\mathbf{S}(t_k^{\mathrm{R}})\mathbf{K}_k'$$

where

$$\nu(t_k^{\mathrm{R}}) = \mathbf{z}(t_k^{\mathrm{R}}) - \hat{\mathbf{z}}(t_k^{\mathrm{R}})$$
$$\mathbf{K}_k = \mathbf{P}_{xz}\mathbf{S}(t_k^{\mathrm{R}})^{-1}$$
$$\mathbf{S}(t_k^{\mathrm{R}}) = \mathbf{R} + \mathbf{P}_{zz}$$
$$\mathbf{P}_{xz} = \sum_{i=1}^{2n_{\mathbf{x}}+1} w^i\tilde{\mathbf{x}}^i(\hat{t}_k^i|\hat{t}_{k-1}^i)\tilde{\mathbf{z}}^i(t_k^{\mathrm{R}})'$$
$$\mathbf{P}_{zz} = \sum_{i=1}^{2n_{\mathbf{x}}+1} w^i[\tilde{\mathbf{z}}^i(t_k^{\mathrm{R}})\tilde{\mathbf{z}}^i(t_k^{\mathrm{R}})']$$
$$\tilde{\mathbf{z}}^i(t_k^{\mathrm{R}}) = \hat{\mathbf{z}}^i(t_k^{\mathrm{R}}) - \hat{\mathbf{z}}(t_k^{\mathrm{R}})$$
$$\tilde{\mathbf{x}}^i(\hat{t}_k^i|\hat{t}_{k-1}^i) = \hat{\mathbf{x}}^i(\hat{t}_k^i|\hat{t}_{k-1}^i) - \hat{\mathbf{x}}(\hat{t}_k|\hat{t}_{k-1})$$

(3500m,0m), respectively. The transmitter emits a CW signal with frequency 1000Hz. The sampling interval of the receiver is $T = 1$s. The measurement errors of bearing and Doppler shifted frequency at receiver are assumed Gaussians with standard deviations $\sigma_b = 1^{\mathrm{o}}$ and $\sigma_f = 0.25$Hz, respectively. The sound propagation speed in water is $c^{\mathrm{p}} = 1484$m/s.

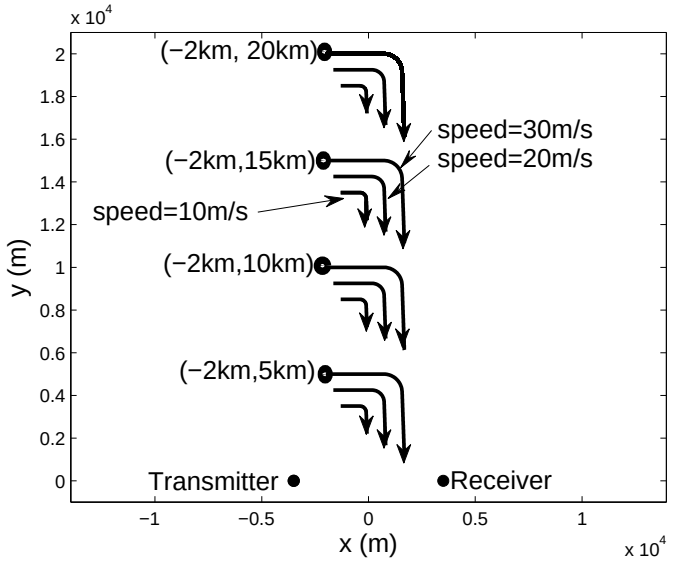

Fig. 3. Test scenarios.

The following two algorithms are used in testing:

- IMM-UKF: The mode-matched filters are UKF. They estimate target position and velocity only. The propagation delay is not taken into consideration at all. The Doppler shifted frequency in the measurement model is based on (37) which is commonly used in multistatic radar tracking

system. The target times are taken as the signal reception times by the receiver.

- IMM-UGHF-NJ: This is the new algorithm proposed in this paper. The propagation delay is taken into consideration in the state estimation, and the target times attached to the target trajectory are estimated from multiple UGHF-NJs.

One CV model and two CT models (CT-L and CT-H) are used in both IMM estimators. The CT-L and CT-H have low and high turn rate process noises, respectively. This setup can provide a fast turn rate adaptation during model switching [4]. The initial mode probabilities for the three models are 1/3. The probability transition matrix Π^3 is

$$\Pi^3 = \begin{bmatrix} 0.950 & 0.025 & 0.025 \\ 0.025 & 0.950 & 0.025 \\ 0.025 & 0.025 & 0.950 \end{bmatrix} \tag{41}$$

The measurement error covariance $\mathbf{R}$ is

$$\mathbf{R} = \mathrm{diag}[(1^{\mathrm{o}})^2 \ (0.25\mathrm{Hz})^2] \tag{42}$$

In the IMM-UGHF-NJ, the process noise covariances $\mathbf{q}^{\mathrm{CV}}$, $\mathbf{q}^{\mathrm{CT\text{-}L}}$ and $\mathbf{q}^{\mathrm{CT\text{-}H}}$ are, respectively,

$$\mathbf{q}^{\mathrm{CV}} = \mathrm{diag}[(0.1\mathrm{m/s}^2)^2 \ (0.1\mathrm{m/s}^2)^2 \ (0.1\mathrm{s})^2] \tag{43}$$

$$\mathbf{q}^{\mathrm{CT\text{-}L}} = \mathrm{diag}[(0.1\mathrm{m/s}^2)^2 \ (0.1\mathrm{m/s}^2)^2 \ (0.1^{\mathrm{o}})^2 \ (0.1\mathrm{s})^2] \tag{44}$$

$$\mathbf{q}^{\mathrm{CT\text{-}H}} = \mathrm{diag}[(0.1\mathrm{m/s}^2)^2 \ (0.1\mathrm{m/s}^2)^2 \ (1^{\mathrm{o}})^2 \ (0.1\mathrm{s})^2] \tag{45}$$

and κ is set to 1 in all $\mathrm{SigPt}(\cdot)$ (see the Appendix), and $\sigma_{t_k^{\mathrm{R}}}$ is set to 0.1s in Algorithm 2. The initial state estimates are

$$\hat{\mathbf{x}}^{\mathrm{CV}}(t_0) = [\hat{r}_0 \sin b_0 \ \hat{r}_0 \cos b_0 \ \hat{\dot{x}}_0 \ \hat{\dot{y}}_0 \ \hat{t}_0]' \tag{46}$$

$$\hat{\mathbf{x}}^{\mathrm{CT\text{-}L}}(t_0) = [\hat{r}_0 \sin b_0 \ \hat{r}_0 \cos b_0 \ \hat{\dot{x}}_0 \ \hat{\dot{y}}_0 \ 0.1^{\mathrm{o}} \ \hat{t}_0]' \tag{47}$$

$$\hat{\mathbf{x}}^{\mathrm{CT\text{-}H}}(t_0) = \hat{\mathbf{x}}^{\mathrm{CT\text{-}L}}(t_0) \tag{48}$$

where

$$\hat{r}_0 \ \sim \ \mathcal{N}(r_0^{\mathrm{R}}, \sigma_r^2) \tag{49}$$

$$b_0 \ = \ b(t_0^{\mathrm{R}}) \tag{50}$$

$$\hat{\dot{x}}_0 \ \sim \ \mathcal{N}(\dot{x}_0, \sigma_{\dot{x}}^2) \tag{51}$$

$$\hat{\dot{y}}_0 \ \sim \ \mathcal{N}(\dot{y}_0, \sigma_{\dot{y}}^2) \tag{52}$$

$$\hat{t}_0 \;=\; t_0^{\mathrm{R}} - \hat{r}_0/c^{\mathrm{p}} \tag{53}$$

with r_0^{R} the true value of the range from the target at time t_0 to the receiver at time t_0^{R}, $\sigma_r = 400$m, and $b(t_0^{\mathrm{R}})$ is the measured bearing at time t_0^{R}, $\dot{x}_0$ and $\dot{y}_0$ are the true target velocities, and $\sigma_{\dot{x}} = \sigma_{\dot{y}} = 4$m/s. The initial state error covariances for the three models are

$$\mathbf{P}^{\mathrm{CV}}(t_0) = \begin{bmatrix} P_{xx} & P_{xy} & 0 & 0 & 0 \\ P_{yx} & P_{yy} & 0 & 0 & 0 \\ 0 & 0 & \sigma_{\dot{x}}^2 & 0 & 0 \\ 0 & 0 & 0 & \sigma_{\dot{y}}^2 & 0 \\ 0 & 0 & 0 & 0 & (\sigma_r/c^{\mathrm{p}})^2 \end{bmatrix} \tag{54}$$

$$\begin{aligned} &\mathbf{P}^{\text{CT-L}}(t_0) = \mathbf{P}^{\text{CT-H}}(t_0) \\ &= \begin{bmatrix} P_{xx} & P_{xy} & 0 & 0 & 0 & 0 \\ P_{yx} & P_{yy} & 0 & 0 & 0 & 0 \\ 0 & 0 & \sigma_{\dot{x}}^2 & 0 & 0 & 0 \\ 0 & 0 & 0 & \sigma_{\dot{y}}^2 & 0 & 0 \\ 0 & 0 & 0 & 0 & (0.02^{\mathrm{o}})^2 & 0 \\ 0 & 0 & 0 & 0 & 0 & (\sigma_r/c^{\mathrm{p}})^2 \end{bmatrix} \end{aligned} \tag{55}$$

where

$$P_{xx} \;=\; (\hat{r}_0\sigma_b \cos b_0)^2 + (\sigma_r \sin b_0)^2 \tag{56}$$

$$P_{yy} \;=\; (\hat{r}_0\sigma_b \sin b_0)^2 + (\sigma_r \cos b_0)^2 \tag{57}$$

$$P_{xy} \;=\; P_{yx} = (\sigma_r^2 - \hat{r}_0^2\sigma_b^2) \sin b_0 \cos b_0 \tag{58}$$

The parameters in the IMM-UKF, including the process noise covariances, initial states and initial state error covariances are the same as the IMM-UGHF-NJ, but the elements corresponding to the target time are removed.

The simulation results present the root mean square errors (RMSE) of the estimated target positions and speeds obtained from 100 Monte Carlo runs. The estimated position and speed errors at time $\hat{t}_k$ are computed by

$$\mathrm{pos}^{\mathrm{err}}(\hat{t}_k) = \sqrt{[\hat{x}(\hat{t}_k) - x(\hat{t}_k)]^2 + [\hat{y}(\hat{t}_k) - y(\hat{t}_k)]^2} \tag{59}$$

$$\mathrm{sp}^{\mathrm{err}}(\hat{t}_k) = \sqrt{[\hat{\dot{x}}(\hat{t}_k) - \dot{x}(\hat{t}_k)]^2 + [\hat{\dot{y}}(\hat{t}_k) - \dot{y}(\hat{t}_k)]^2} \tag{60}$$

where $\hat{x}(\hat{t}_k)$, $\hat{y}(\hat{t}_k)$, $\hat{\dot{x}}(\hat{t}_k)$ and $\hat{\dot{y}}(\hat{t}_k)$ are the estimated target positions and velocities in the x and y coordinates respectively, $x(\hat{t}_k)$, $y(\hat{t}_k)$, $\dot{x}(\hat{t}_k)$ and $\dot{y}(\hat{t}_k)$ are the true target positions and velocities in

the x and y coordinates respectively, and $\hat{t}_k$ is the estimated target time in estimation cycle k.

Tables I and II show the averages of position and speed RMSE for the two algorithms for the twelve simulated targets from the four categories displayed in Fig. 3. Figs. 4–7 show the position RMSE versus time of the two algorithms for four simulated targets, one from each category, respectively. They are the targets in the range between 0–5km with speed 30m/s, range between 5–10km with speed 10m/s, range between 10–15km with speed 20m/s and range between 15–20km with speed 30m/s. It can be seen that the IMM-UGHF-NJ outperforms the IMM-UKF for all targets. The accuracy improvement is target range and speed dependent. A faster and longer range target has more improvement than a slower one at a shorter range. This is because that estimation error of the IMM-UKF depends on the target speed and propagation delay τ_k^{R} (details can be found in Section V-C of [12]). The range from the target to the receiver is proportional to the propagation delay. From the results we can say that the estimation error without considering propagation delay is significant, especially for a long range target or a fast target (such as a speed boat or torpedo).

TABLE I
AVERAGES OF POSITION RMSE

Target Range (km)	Target Speed (m/s)	IMM-UKF (m)	IMM-UGHF-NJ (m)	Improv. (m)
0–5	10	412.6	411.9	0.7
	20	397.9	375.4	22.5
	30	319.3	281.8	37.5
5–10	10	406.5	400.8	5.7
	20	387.4	336.0	51.4
	30	438.4	325.2	113.2
10–15	10	413.1	401.5	11.6
	20	489.9	428.2	61.7
	30	523.0	369.7	153.3
15–20	10	436.8	412.7	24.1
	20	481.0	407.5	73.5
	30	614.2	399.5	214.7

The maneuvering mode probabilities of the two IMM filters are also investigated. Figs. 8–11 show the sum of the mode probabilities of the two CT models (which represents the target maneuvering probability) versus time for the four targets, respectively. It can be seen that the maneuvering probability for both filters increases when the target is maneuvering. The IMM-UGHF-NJ reacts faster than the IMM-UKF. A delay in the model switching for a long range target (> 5km) is observed. However, the mode probability does not match the ground truth very well when the target is in CV motion. This is because the turn rate ω in CT models can adapt to a small value when the target is in CV motion.

TABLE II
AVERAGES OF SPEED RMSE

Target Range (km)	Target Speed (m/s)	IMM-UKF (m/s)	IMM-UGHF-NJ (m/s)	Improv. (m/s)
0–5	10	1.9	1.8	0.1
	20	2.4	2.0	0.4
	30	2.9	2.4	0.5
5–10	10	2.0	1.8	0.2
	20	2.7	1.9	0.8
	30	3.8	2.1	1.7
10–15	10	2.4	1.9	0.5
	20	3.5	1.9	1.6
	30	5.0	2.2	2.8
15–20	10	3.0	2.4	0.6
	20	4.3	2.0	2.3
	30	6.2	2.1	4.2

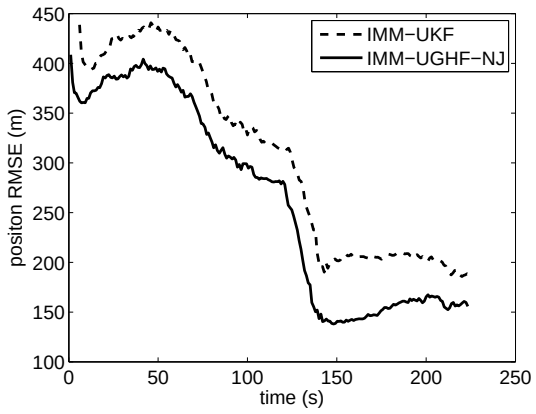

Fig. 4. Position estimate RMSE versus time for the target with speed=30m/s and range less than 5km.

To evaluate the consistency of the IMM-UGHF-NJ and IMM-UKF, the average normalized estimation error squared (NEES) is evaluated. The average (2D) position NEES at time $\hat{t}_k$ for N Monte Carlo runs is [1]

$$\bar{\epsilon}(\hat{t}_k) = \frac{1}{2N}\sum_{i=1}^{N} \tilde{\mathbf{x}}^i_{1:2}(\hat{t}_k)'[\mathbf{P}^i_{1:2,1:2}(\hat{t}_k)]^{-1}\tilde{\mathbf{x}}^i_{1:2}(\hat{t}_k) \tag{61}$$

where i the run index, $\mathbf{P}^i_{1:2,1:2}(\hat{t}_k)$ is the position estimate error covariance submatrix at the estimated target time $\hat{t}_k$, and

$$\tilde{\mathbf{x}}_{1:2}(\hat{t}_k) = \hat{\mathbf{x}}_{1:2}(\hat{t}_k) - \mathbf{x}_{1:2}(\hat{t}_k) \tag{62}$$

The two-sided 95% probability region for a 200 degrees of freedom ($N = 100$, dimension of $\mathbf{x}_{1:2} = 2$) chi-square random variable is [162, 241.2]. Dividing by 200, the average NEES interval is [0.81, 1.21].

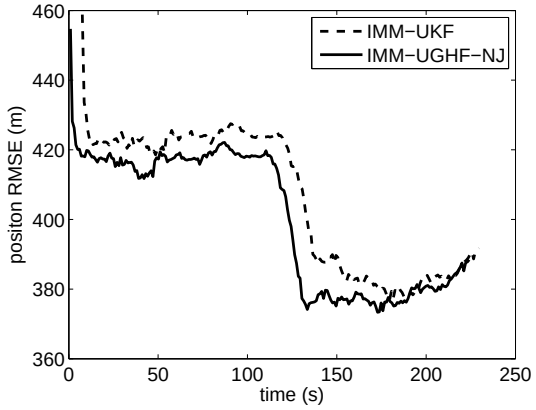

Fig. 5. Position estimate RMSE versus time for the target with speed=10m/s and range 5–10km.

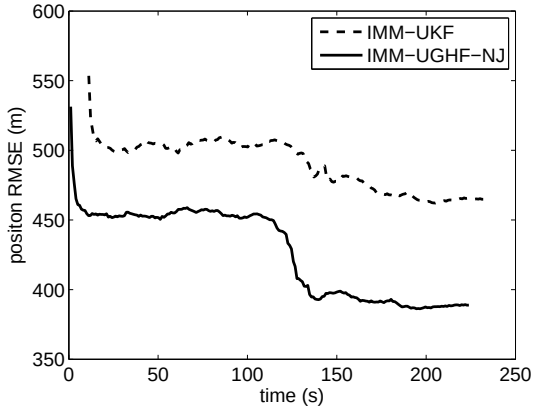

Fig. 6. Position estimate RMSE versus time for the target with speed=20m/s and range 10–15km.

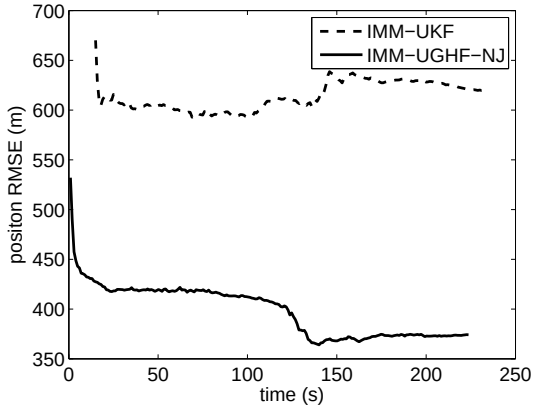

Fig. 7. Position estimate RMSE versus time for the target with speed=30m/s and range 15–20km.

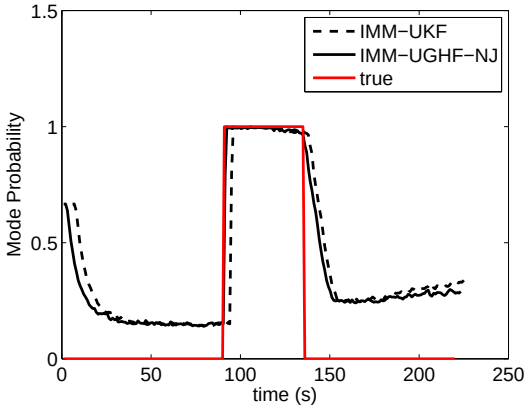

Fig. 8. Maneuvering probability versus time for target with speed=30m/s and range less than 5km.

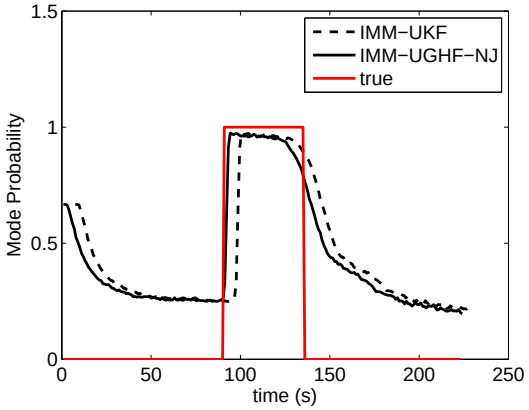

Fig. 9. Maneuvering probability versus time for target with speed=10m/s and range 5–10km.

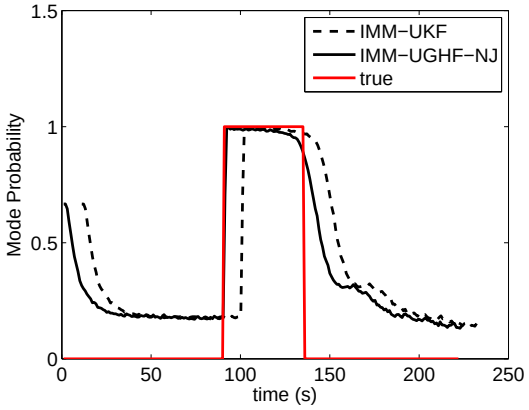

Fig. 10. Maneuvering probability versus time for target with speed=20m/s and range 10–15km.

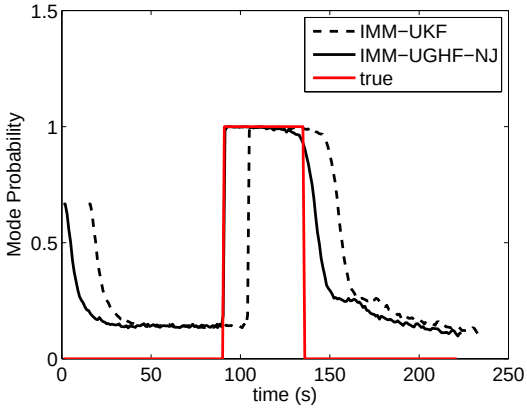

Fig. 11. Maneuvering probability versus time for target with speed=30m/s and range 15–20km.

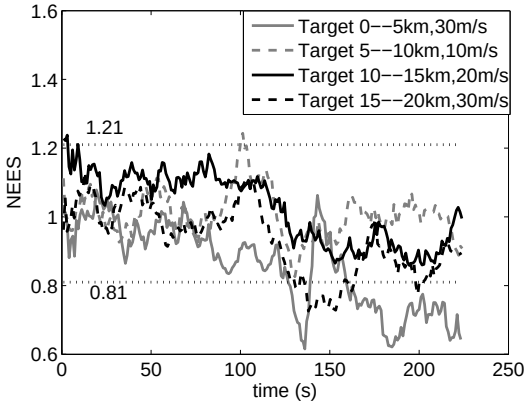

Fig. 12. Four targets position NEES versus time for the IMM-UGHF-NJ.

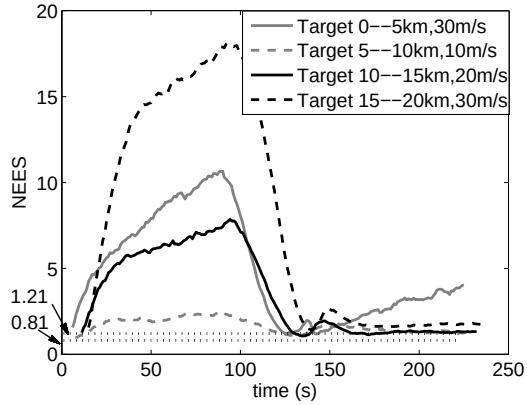

Fig. 13. Four target position NEES versus time for the IMM-UKF.

Fig. 12 shows the average position NEES versus time of the IMM-UGHF-NJ for the four targets

with expected value 1. It can be seen that most of the position NEES are within the interval [0.81, 1.21]. There are two exception cases out of the interval. One is at the model switching times which are around 90s and 135s. Another one is at the ending part of the near range target (0–5km, 30m/s). When the target is switching between the CV and CT motions, the IMM-UGHF-NJ cannot adapt to the correct model immediately, and this causes short delay in the maneuver start and maneuver end, but these delays are shorter than for the IMM-UKF. For the near range target (0–5km, 30m/s), the NEES is below the lower bound 0.81 at the ending part ($t > 160$s). We can observe from Fig. 8 that the maneuvering probability is greater than 0.24 when $t >$160s. It is apparently worse than for the other three targets shown in Figs. 9–11. This is caused by the marginal observability of the CV motion model from the measurements, and results in the maneuvering probability (sum of the probabilities of CT models) not small enough. The error covariance of the combined estimate is too large (pessimistic) when the contribution of the incorrect models (the maneuvering models with probability around 0.25) cannot be overlooked. The small NEES is therefore caused by this large error covariance.

Fig. 13 shows the NEES of the IMM-UKF for the same four targets. All of them are above the upper bound 1.21. Obviously, the IMM-UKF provides biased estimation without considering propagation delay.

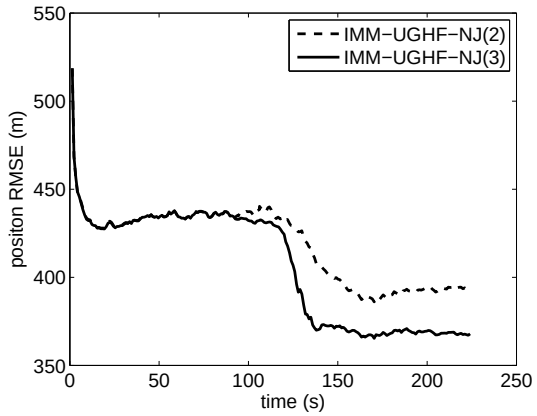

Fig. 14. Position estimate RMSE versus time of the IMM-UGHF-NJ using two-model and three-model for the target with speed=20m/s and range 10–15km.

We also compare the results of using three models and two models in the IMM-UGHF-NJ. The models and parameters in the three-model configuration have been defined before. The two-model IMM-UGHF-NJ uses one CV model and one CT model. Their initial mode probabilities are 1/2, and

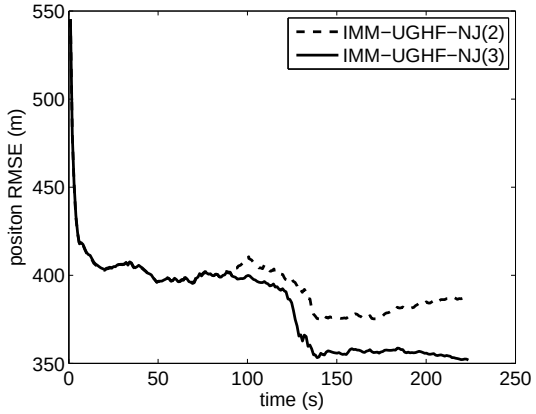

Fig. 15. Position estimate RMSE versus time of the IMM-UGHF-NJ using two-model and three-model for the target with speed=30m/s and range 15–20km.

the probability transition matrix Π^2 is

$$\Pi^2 = \begin{bmatrix} 0.95 & 0.05 \\ 0.05 & 0.95 \end{bmatrix} \tag{63}$$

The process noises the initial states in the two-model estimator are set as the same for the CV and CT in the three-model case, except the process noise variance on turn rate is set as $(0.5^{\circ}/\mathrm{s})^2$ (intermediate value between those in the CT-L and CT-H models). Figs. 14 and 15 show the position estimate RMSE versus time of using two models and three models for the two targets (10–15km, 20m/s and 15–20km, 30m/s). It can be seen that there is no difference in the first leg ($t < 90$s) between two-model and three-model IMM-UGHF-NJs. Once the targets start maneuvering, the three-model IMM-UGHF-NJ outperforms the two-model version. This is due to the model CT-H with high process noise on the turn rate. It allows the turn rate to adapt to the correct value quickly during model switchings. Meanwhile, the CT-L model with slow change in turn rate can balance the CT-H after model switching.

V. Conclusions

This paper developed the IMM-UGHF-NJ filter to track maneuvering targets using bistatic CW-CAS in the presence of propagation delay. The IMM-UGHF-NJ can overcome the two challenges of this tracking problem, namely, the implicit state transition model and absence of analytical expression of the Doppler shifted frequency in the measurement model. Simulation tests were conducted on targets with different ranges and speeds. Results show that the IMM-UGHF-NJ outperforms the IMM-UKF which does not take the propagation delay into consideration. It is also found that the estimate accuracy improvement of the IMM-UGHF-NJ over the IMM-UKF is more significant for a longer range or

a higher speed target. Such a target (for example a speed boat or a torpedo) needs an appropriate filter (IMM-UGHF-NJ) to handle the propagation delay. A statistical study of the results was also conducted through the NEES. The results show that the IMM-UGHF-NJ is a consistent filter in most of the cases, except the situations when the target motion uncertainty cannot be well observed from measurements. The NEES results of the IMM-UKF are far above the upper bound because of its biased estimation due to ignoring the propagation delay.

APPENDIX

The three algorithms $\mathrm{SigPt}(\cdot)$, $\mathrm{GaussN}(\cdot)$ and $\mathrm{NJ}(\cdot)$ used in IMM-UGHF-NJ are given next.

a) $\mathrm{SigPt}(\cdot)$ generates the sigma points for a random variable $\mathbf{x}$ with covariance $\mathbf{P_x}$ [7].

$$[\mathbf{x}^i, w^i] = \mathrm{SigPt}(\mathbf{x}, \mathbf{P_x}, \kappa) \qquad i = 1, \ldots, 2n_\mathbf{x} + 1 \tag{64}$$

where

$$\mathbf{x}^1 = \mathbf{x} \tag{65}$$

$$\mathbf{x}^i = \mathbf{x} + \left[\sqrt{(n_\mathbf{x} + \kappa)\mathbf{P_x}}\,\right]_{i-1} \qquad i = 2, \cdots, n_\mathbf{x} + 1 \tag{66}$$

$$\mathbf{x}^i = \mathbf{x} - \left[\sqrt{(n_\mathbf{x} + \kappa)\mathbf{P_x}}\,\right]_{i-n_\mathbf{x}-1} \qquad i = n_\mathbf{x} + 2, \cdots, 2n_\mathbf{x} + 1 \tag{67}$$

$$w_0 = \frac{\kappa}{n_\mathbf{x} + \kappa} \qquad i = 1 \tag{68}$$

$$w_i = \frac{1}{2(n_\mathbf{x} + \kappa)} \qquad i = 2, \cdots, 2n_\mathbf{x} + 1 \tag{69}$$

where $n_\mathbf{x}$ is the dimension of $\mathbf{x}$, $\left[\sqrt{(n_\mathbf{x} + \kappa)\mathbf{P_x}}\,\right]_{i^*}$ indicates the i^*th column of the matrix $[\cdot]$, and κ is a scalar that determines the spread of sigma points.

b) $\mathrm{GaussN}(\cdot)$ is a Gauss-Newton algorithm to obtain the solution of an implicit equation $\mathbf{g}(\cdot) = \mathbf{0}$ iteratively [11][12] and yields

$$\hat{\mathbf{x}}_1 = \mathrm{GaussN}[\mathbf{g}(\mathbf{x}_1, \mathbf{x}_0)] \tag{70}$$

where $\mathbf{x}_0$ is known. The iteration procedure is

$$\hat{\mathbf{x}}_1^{j+1} = \hat{\mathbf{x}}_1^j + (\mathbf{A}^j)^{-1}\mathbf{g}(\hat{\mathbf{x}}_1^j, \mathbf{x}_0) \tag{71}$$

where j is the iteration index, $\mathbf{A}^j$ is the Jacobian matrix defined by

$$\mathbf{A}^j = \frac{\partial \mathbf{g}[(\hat{\mathbf{x}}_1^j, \mathbf{x}_0)]}{\partial \hat{\mathbf{x}}_1^j} \tag{72}$$

c) $\mathrm{NJ}(\cdot)$ calculates the Jacobian (or derivative) $\mathbf{H}$ of a function

$$\mathbf{z} = \mathbf{h}(\mathbf{x}) \tag{73}$$

at a point of interest $\mathbf{x}_0$ numerically [8][13][9]. There is no analytical form for $\mathbf{h}(\cdot)$, but $\mathbf{z}$ can be obtained through numerical method from a given $\mathbf{x}$. The Jacobian is

$$\mathbf{H} = \mathrm{NJ}[\{\mathbf{x}^i\}, \{\mathbf{z}^i\}, \{w^i\}] \tag{74}$$

where $\{\mathbf{x}^i\}$ is the sigma point set around $\mathbf{x}_0$ generated from a very small covariance, $\{\mathbf{z}^i\}$ is its corresponding set after transformation and $\{w^i\}$ is the set of weights. The NJ is implementing through the following steps:

1) Form the sigma point set

$$\bar{\mathbf{X}} = \begin{bmatrix} \mathbf{x}^1 & \mathbf{x}^2 & \cdots & \mathbf{x}^{2n_{\mathbf{x}}+1} \\ 1 & 1 & \cdots & 1 \end{bmatrix} - \begin{bmatrix} \mathbf{x}^1 \\ 0 \end{bmatrix} \tag{75}$$

$$\mathbf{Z} = \begin{bmatrix} \bar{\mathbf{z}}^1 \\ \bar{\mathbf{z}}^2 \\ \vdots \\ \bar{\mathbf{z}}^l \end{bmatrix} = \begin{bmatrix} \mathbf{z}^1 & \mathbf{z}^2 & \cdots & \mathbf{z}^{2n_{\mathbf{x}}+1} \end{bmatrix} \tag{76}$$

where $\mathbf{x}^1 = \mathbf{x}_0$, and l is the dimension of $\mathbf{z}$.

2) Estimate $\mathbf{H}$ using the weighted least squares (WLS) algorithm

$$\mathbf{a}^j = (\bar{\mathbf{X}}\mathbf{W}\bar{\mathbf{X}}')^{-1}\bar{\mathbf{X}}\mathbf{W}(\bar{\mathbf{z}}^j)' \tag{77}$$

$$\hat{\bar{\mathbf{H}}} = \begin{bmatrix} \mathbf{a}^1 & \mathbf{a}^2 & \cdots & \mathbf{a}^l \end{bmatrix}' \tag{78}$$

$$\hat{\mathbf{H}} = \hat{\bar{\mathbf{H}}}(1 : l, 1 : n_{\mathbf{x}}) \tag{79}$$

where $\mathbf{W} = \mathrm{diag}(\{w^i\})$, $j \in \{1, \ldots, l\}$, and $\hat{\mathbf{H}}$ is $\hat{\bar{\mathbf{H}}}$ without the last column.

REFERENCES

[1] Bar-Shalom, Y., Li, X.R. and Kirubarajan, T., *Estimation with Applications to Tracking and Navigation: Theory, Algorithms and Software*, New York: Wiley, 2001.

[2] Bar-Shalom, Y., Willett, P.K. and Tian, X., *Tracking and Data Fusion: A Handbook of Algorithms*, YBS Publishing, 2011.

[3] DeFerrari, H.A., "The Application of m-Sequences to Bi-static Active Sonar", *Journal of the Acoustical Society of America*, 114(4):2399-2400, 2003.

[4] Huang, H.A.J., Bar-Shalom, Y., Yang, R. and Ng, G.W., "Tracking a maneuvering target using two heterogeneous passive sensors on a single stationary platform with IMM estimation", *submitted to Journal of Advances in Information Fusion*, November 2015.

[5] Grimmett, D., Wakayama, C., "Multistatic Tracking for Continous Active Sonar using Doppler-Bearing Measurements", *Proc. 16th International Conference on Information Fusion*, Istanbul, Turkey, Jul. 2013.

[6] Jauffret, C., Pérez, A.-C., Blanc-Benon, P. and Tanguy, H., "Doppler-only Target Motion Analysis in a High Duty Cycle Sonar System", *Proc. 19th International Conference on Information Fusion*, Heidelburg, Germany, Jul. 2016.

[7] Julier, S.J. and Uhlmann, J.K., "A new extension of the Kalman filter to nonlinear systems", *Proceedings of AeroSense: The 11th International Symposium on Aerospace/Defence Sensing, Simulation and Controls*, Apr. 1997.

[8] Xiong, Y.B., Zhong, X.H. and Yang, R., "The linear fitting Kalman filter for nonlinear tracking", *Proceedings of the 5th Asia-Pacific Conference on Synthetic Aperture Radar*, Singapore, Sep. 2015.

[9] Xiong, Y.B. and Zhong, X.H., "Linear fitting Kalman filter", *IET Signal Processing*, 10(4):404–412, Jun. 2016.

[10] Yang, T.E., "Acoustic Dopplergram for Intruder Defense", *Proceedings of IEEE Oceans 2007*, Vancouver, BC, Canada, Sep. 2007.

[11] Yang, R., Bar-Shalom, Y., Huang, J.A.H. and Ng, G.W., "Interacting multiple model unscented Gauss-Helmert filter for bearings-only tracking with state-dependent propagation delay", *Proc. 17th International Conference on Information Fusion*, Salamanca, Spain, Jul. 2014.

[12] Yang, R., Bar-Shalom, Y., Huang, J.A.H. and Ng, G.W., "UGHF for acoustic tracking with state-dependent propagation delay", *IEEE Transactions on Aerospace and Electronic Systems*, 51(3):1747–1761, Aug. 2015.

[13] Yang, R. and Bar-Shalom, Y. "Comparison of altitude estimation using 2D and 3D radars over spherical Earth", *Proceedings of IEEE Aerospace Conference 2016*, Big Sky, MT, USA, Mar. 2016.

[14] Yang, R., Bar-Shalom, Y. and Ng, G.W., "Bearings-only tracking with fusion from heterogenous passive sensors: ESM/EO and acoustic," *Proc. 18th International Conference on Information Fusion*, Washington, DC, Jul. 2015.

[15] Yang, R., Bar-Shalom, Y. and Ng, G.W., "Bearings-Only Tracking with Fusion from Heterogenous Passive Sensors: ESM/EO and Acoustic", *Journal of Advances in Information Fusion*, 11(2), Dec. 2016.

[16] Yuan, T., Bar-Shalom, Y., Willett, P., Mozeson, E., Pollak, S. and Hardiman D., "A multiple IMM estimation approach with unbiased mixing for thrusting projectiles", *IEEE Transactions on Aerospace and Electronic Systems*, 48(4):3250-3267, Oct. 2012.